



Modelling chordwise-varying porosity to reduce aerofoil-turbulence interaction noise

Lorna J. Ayton* and Matthew J. Colbrook †

Department of Applied Mathematics and Theoretical Physics, University of Cambridge

Thomas F. Geyer‡

Aeroacoustics Group, Brandenburg Technical University of Cottbus

Paruchuri Chaitanya§

Engineering and Physical Sciences, University of Southampton

Ennes Sarradj¶

Department of Technical Acoustics, Technical University Berlin

We consider a finite perforated plate and study the effects of smoothly varying chordwise porosity on turbulence-aerofoil interaction noise. To study this problem, we use a novel Mathieu function collocation method, rather than a traditional Wiener–Hopf approach which would be unable to deal with chordwise varying quantities. Our main focus is on two bio-inspired porosity distributions, which are modelled based on air flow resistance data from the wings of barn owls and common buzzards. As expected, trailing-edge noise is much reduced for the owl-like distribution. However, and perhaps surprisingly, so too is leading-edge noise, despite both wings having similar porosity values at the leading edge. We then consider a general monotonic variation. Our study indicates that there may be a significant acoustic impact of *how* the porosity is distributed along the whole chord of the plate (i.e. not just its values at the scattering edges). Indeed, a plate whose porosity continuously decreases from the trailing edge to a zero-porosity leading edge can, in fact, generate lower levels of trailing-edge noise than a plate whose porosity remains constant at the trailing-edge value.

I. Introduction

Porosity adaptations of traditional rigid impermeable aerofoils offer an opportunity for reducing the interaction noise of aerofoil-turbulence [1–4]. Both leading-edge noise (caused by upstream turbulence impinging on the aerofoil) and trailing-edge noise (caused by boundary layer turbulence scattering off the trailing edge) can be reduced by replacing an impermeable aerofoil with a fully porous aerofoil [5], or partially porous aerofoil [6–8]. However, previous theoretical [1], numerical [9–11] and experimental [5, 6] investigations have focused on materials with *uniform* porosity or on chordwise variations achieved only through the use of partially porous aerofoils. This latter case causes an unavoidable and instantaneous variation of the boundary from impermeable to permeable, where additional noise is generated by edge scattering [1, 12]. Partially porous aerofoils are very important since one can hope to balance between acoustic and aerodynamic needs as fully porous aerofoils have significant aerodynamic penalties [5]. The steady aerodynamics of partially porous aerofoils have previously been predicted theoretically by [13], which has been extended to aerofoils with porosity gradients by [14].

The goal of this paper is to investigate how *porosity gradients* effect the noise generated by aerofoil-turbulence interaction. We do this by studying arbitrary variations in porosity along a finite perforated flat plate, modelling a thin permeable aerofoil. The scattered acoustic field is computed using a novel spectral collocation method [15–18] based on Mathieu functions. We first focus on monotonic porosity distributions as done so in [19] inspired by two species

*EPSRC Early Career Fellow, Department of Applied Mathematics and Theoretical Physics, University of Cambridge, email: l.j.ayton@damtp.cam.ac.uk

†Junior Research Fellow, Department of Applied Mathematics and Theoretical Physics, University of Cambridge, email: m.colbrook@damtp.cam.ac.uk

‡Brandenburg University of Technology, Cottbus, Germany

§University of Southampton, Southampton, UK

¶Technical University Berlin, Berlin, Germany

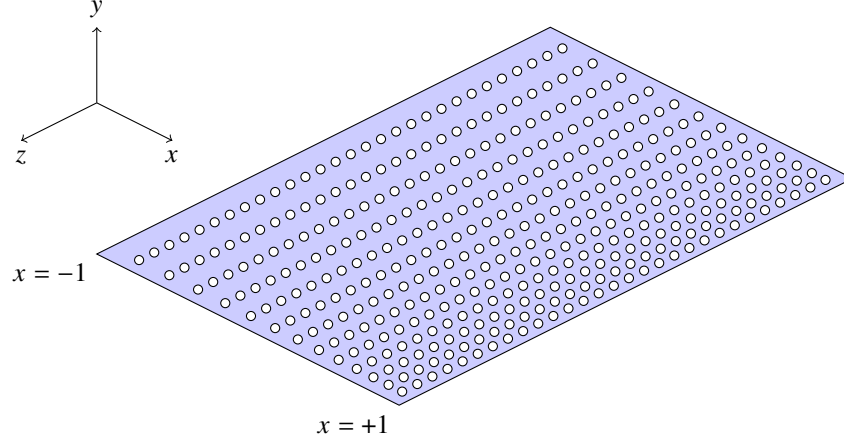


Fig. 1 Schematic of the variable porosity plate with edges at $x = -1$ and $x = 1$. The plate extends infinitely in the spanwise (z) direction.

of birds: barn owls (*tyto alba*), known for their silent flight [20, 21], and common buzzards (*buteo buteo*). Both are modelled from air flow resistance data obtained from the wings of the two species. As expected, trailing-edge noise is predicted to be much reduced for the owl-like distribution (porosity is a known contributor to the ability of owls to fly silently and hunt prey). A study into general monotonic variation indicates that there may be a significant acoustic impact of *how* the porosity is distributed along the whole chord of the plate, not just its values at the scattering edges. Through this investigation, it is found that a plate whose porosity continuously decreases from the trailing edge to a zero-porosity leading edge can, in fact, generate lower levels of trailing-edge noise than a plate whose porosity remains constant at the trailing-edge value. Code for the numerical method can be found at [22].

II. Mathematical Model

Here we briefly discuss the core method for calculating the scattered field due to an acoustic source interacting with a plate with an arbitrary porosity distribution. Consider an incident field impinging on a flat plate situated at $-1 \leq x \leq 1$ and $y = 0$, where lengths have been non-dimensionalised by semi-chord. The plate is in uniform horizontal flow, with velocities non-dimensionalised by the low-Mach number far-upstream mean flow velocity. The incident field will have velocity potential denoted by ϕ_I and the scattered field by ϕ . The incident pressure field is given by $p_I = -\rho_f \frac{D\phi}{Dt}$, where ρ_f is the mean fluid density and $\frac{D\phi}{Dt}$ denotes the material derivative. Pressure shall henceforth be non-dimensionalised by $\rho_f c_0^2$ with c_0 denoting the speed of sound, so that throughout we deal with dimensionless fields ϕ_I and ϕ .

We assume that ϕ has the usual time dependence $e^{-i\omega t}$ (which will be omitted throughout), and hence for low Mach number flow, ϕ satisfies the Helmholtz equation

$$\left(\frac{\partial^2}{\partial x^2} + \frac{\partial^2}{\partial y^2} + k_0^2 \right) \phi = 0,$$

where $k_0 = \omega/c_0$ is the acoustic wavenumber for angular frequency ω . We apply an impedance boundary condition given by

$$\frac{\partial \phi}{\partial y} + \frac{\partial \phi_I}{\partial y} = \mu(x) (\phi_u - \phi_l) = \mu(x) [\phi](x), \quad (1)$$

to model the effects of the porous plate, where $\mu = \alpha_H K_R / (\pi r^2)$ is the porosity parameter [23, 24]. Here K_R is the Rayleigh conductivity [25], which for evenly-spaced circular apertures of radius r , is given by $K_R = 2r$. The fractional open area is α_H [26]. Such a model is valid for $\alpha_H^2 \ll 1$, and $k_0 r \ll 1$. We use the notation ϕ_u and ϕ_l to denote the values of the field just above and just below the plate respectively, and the jump in ϕ across the plate is denoted by $[\phi]$. Note that, unlike previous theoretical models [1, 23], we allow the porosity parameter $\mu(x)$ to *vary along the plate*. Finally, the scattered field is required to satisfy the Sommerfeld radiation condition for outgoing waves at infinity. Our setup is illustrated in Figure 1.

A. Computing the solution via Mathieu function expansions

Here we solve the problem using the Mathieu function collocation method of [15], which provides an expansion of ϕ in Mathieu functions using separation of variables in elliptic coordinates. When using elliptic coordinates, $x = \cosh(\nu) \cos(\tau)$, $y = \sinh(\nu) \sin(\tau)$, the appropriate domain becomes $\nu \geq 0$ and $\tau \in [0, \pi]$. The Helmholtz equation with homogeneous Dirichlet boundary condition (the continuity condition) along $\{(x, y) : y = 0, |x| > 1\}$ and the Sommerfeld condition at infinity become

$$\begin{cases} \frac{\partial^2 \phi}{\partial \tau^2} + \frac{\partial^2 \phi}{\partial \nu^2} + \frac{\cosh(2\nu) - \cos(2\tau)}{2} k_0^2 \phi = 0, \\ \phi|_{\tau=0} = \phi|_{\tau=\pi} \equiv 0, \\ \lim_{\nu \rightarrow \infty} \nu^{1/2} \left(\frac{\partial}{\partial \nu} - ik_0 \right) \phi(\nu, \tau) = 0. \end{cases}$$

To simplify the formulae, we let $\kappa = k_0^2/4$. Separation of variables leads to the full general solution

$$\phi(\nu, \tau) = \sum_{n=1}^{\infty} a_n \text{se}_n(\tau) \text{Hse}_n(\nu), \quad (2)$$

where a_n are unknown coefficients. Here se_n are sine-elliptic functions, which can be expanded in a rapidly convergent sine series [27]:

$$\text{se}_n(\kappa; \tau) = \text{se}_n(\tau) = \sum_{l=1}^{\infty} B_l^{(n)} \sin(l\tau), \quad (3)$$

where $B_l^{(n)}$ are found by a simple Galerkin method. The functions Hse_n are Mathieu–Hankel functions which can be expanded in a series using Bessel functions [27, 28]:

$$\text{Hse}_n(\nu) = \sum_{l=1}^{\infty} \frac{(-1)^{l+n} B_l^{(n)}}{C_n} \left[J_{l-1}(e^{-\nu} \sqrt{\kappa}) H_{l+p_n}^{(1)}(e^{\nu} \sqrt{\kappa}) - J_{l+p_n}(e^{-\nu} \sqrt{\kappa}) H_{l-1}^{(1)}(e^{\nu} \sqrt{\kappa}) \right], \quad (4)$$

where $p_n = (1 + (-1)^n)/2$. Here, J_n denotes the Bessel function of the first kind of order n and $H_n^{(1)}$ denotes the Hankel function of the first kind of order n . We choose the normalisation constants C_n so that $\text{Hse}'_n(0) = 1$.

Given the Bessel function expansion of $\text{Hse}_n(\nu)$ in (4), we can directly compute the far-field directivity $D(\theta)$ from (2) using asymptotics of Bessel functions. In the appropriate limit, τ becomes the polar angle θ , whereas ν becomes $\cosh^{-1}(r)$ (where (r, θ) denote the usual polar coordinates). This leads to

$$D(\theta) = \sqrt{\frac{2}{\pi k_0}} \sum_{n=1}^{\infty} \frac{a_n B_1^{(n)}}{C_n} \exp\left(\frac{(2p_n - 3)\pi}{4}\right) \text{se}_n(\theta). \quad (5)$$

An advantage of our approach is that we implicitly compute a sine series for the far-field directivity $D(\theta)$ through the sine-elliptic functions $\text{se}_n(\theta)$ given by (3). We also define the total far-field noise, measured in dB, as

$$P = 10 \log_{10} \left(\int_0^{\pi} |D(\theta)|^2 d\theta \right), \quad (6)$$

which may be computed numerically from the series expansion for $D(\theta)$.

We must determine the unknown coefficients a_n in the expansion (2), as required for our particular boundary condition (1). To do so, we adopt a spectral collocation method to calculate their approximate value. Throughout, we denote the approximate coefficients by \tilde{a}_n . We take our general solution (2) and substitute into (1), written in original (x, y) coordinates. We truncate the expansion at N terms to obtain the approximate condition

$$\sum_{n=1}^N \tilde{a}_n \text{se}_n(\cos^{-1}(x)) \left[1 - 2\text{Hse}_n(0) \mu(x) \sqrt{1-x^2} \right] = -\sqrt{1-x^2} \cdot \frac{\partial \phi_1}{\partial y}(x).$$

We now evaluate this at chosen collocation points, $x \in \{\cos((2j-1)\pi/2N) : j = 1, \dots, N\}$, which correspond to Chebyshev points in Cartesian coordinates and equally spaced points in elliptic coordinates [29]. This gives rise to an $N \times N$ linear system for the unknown coefficients $\{\tilde{a}_n\}_{n=1}^N$, which we precondition by rescaling to ensure that each row of the resulting matrix has a constant l^1 vector norm.

III. Experimental measurements

To obtain quantitative data on the permeability of owl wings compared to the wings of other (non-silently flying) birds of prey, measurements of the flow resistance were conducted on a set of prepared wing specimen. For measurements on porous materials according to [30], the materials must be cut into cylindrical samples of constant thickness and tightly fitted into a sample holder. This is obviously not possible for prepared bird wings, which may consist of only a single layer of feathers especially close to the trailing edge (see, for example, the work of [31] and [32]), and hence a special measurement head was constructed. This head is pressed onto the surface of the wings with a defined force, allowing the area of contact between the planar measuring head and the feather surface to be sealed off. Using this measurement head, a defined air flow with a volumetric airflow rate q (in m^3/s) is conducted through the prepared wing (see Figure 2). The air flow resistance R at this position of the wing is then calculated from the resulting static pressure difference across the wing

$$R = \frac{p_u - p_l}{q}. \quad (7)$$

Recall that $\mu(x) = \alpha_H(x)K_R/(\pi r^2)$, where we assume the porosity is created by circular apertures of constant radius, r , and, for a plate with circular apertures, the Rayleigh conductivity of the plate, $K_R = 2r$. However, for an arbitrary material, K_R is defined as $K_R = Q/(\phi_u - \phi_l)$, where $Q = dq/dt$ is the volume flux through the plate. Hence for the wing in harmonic flow, $K_R = \omega^2 \rho_f / R$. We thus have two ways of calculating $\mu(x)$:

$$\mu(x) = \alpha_H(x) \frac{2}{\pi r}, \quad \mu_{\text{exp}}(x) = \alpha_H^{\text{exp}} \omega^2 \rho_f \frac{1}{R} \frac{1}{\pi r_{\text{exp}}^2}, \quad (8)$$

where α_H denotes the open area ratio of circular apertures or radius r in a flat plate, α_H^{exp} denotes the open area ratio of pores of typical radius r_{exp} in a wing, and R is the measured flow air flow resistance. We may thus equate the two to provide values for $\alpha_H(x)$ to input into our model

$$\alpha_H(x) = \frac{\omega^2 \rho_f r \alpha_H^{\text{exp}}}{2Rr_{\text{exp}}^2}. \quad (9)$$

We shall assume that the chordwise variation in (9) arises only due to the air flow resistance, R , and that α_H^{exp} and r_{exp} are constant. According to [23] we take the value $\alpha_H^{\text{exp}} = 0.0014$. Since in [23] lengths are non-dimensionalised by a bending wave number (which does not feature in our analysis since our plate is not flexible), it is more difficult to determine the corresponding value of r_{exp} . We, therefore, turn to detailed measurements made on the wings of barn owls by [33], which results in a value of $r_{\text{exp}} = 5.5 \times 10^{-4}$ m. This arises from supposing for a given barn owl feather there are two fringes per mm [33] (and thus two gaps between the fringes per mm) and the total length of the vane of the feather is between 12.5 cm and 15 cm [34]. Therefore each feather has between 250 and 300 apertures in the chordwise direction. We select r_{exp} as the mid-value, supposing each aperture is $1/275$ of our fixed 15 cm chord.

For the theoretical model, we shall suppose a manufactured flat plate has holes with radius $r = 1$ mm, which is practical to construct, and we use a typical frequency of $\omega = 500\text{Hz}$ to complete our relationship between R and $\alpha_H(x)$ since we wish to focus on low frequency noise reductions. We shall use the same value of the parameter group $\alpha_H^{\text{exp}}/(\pi r_{\text{exp}}^2)$ (which can be viewed as the closed area of the wing) for the owl and buzzard as input to obtain our model, $\alpha_H(x)$. Whilst this is unlikely to be true for the buzzard, it provides an upper bound on the value of α_H to input to our model, as it is clear from detailed wing pictures [35] that the closed area of the buzzard's wing is greater than that for the owl.

IV. Results

A. Bio-inspired distributions

The results from the air flow resistance measurements on the prepared wings are summarised and converted to their corresponding α_H values. Overall, five wings of the barn owl (*tyto alba*) and nine wings of the common buzzard (*buteo buteo*) were investigated to obtain the data used in the present study. Lines of best fit are produced using Matlab's `fit` command (see [19] for the various models considered). From these we shall take the variation which appears most likely in the owl wing to be:

$$\alpha_H^{\text{owl}} = 0.037 + 0.48 \left(\frac{x}{2} + \frac{1}{2} \right), \quad (10)$$

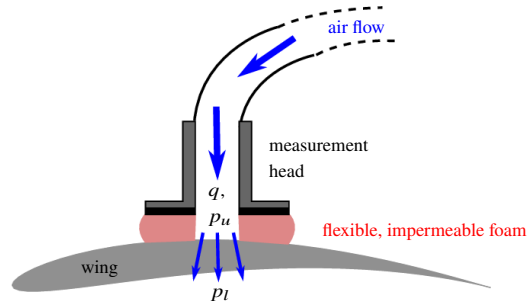


Fig. 2 Setup used to measure the wing air flow resistance R (Eq. (7))

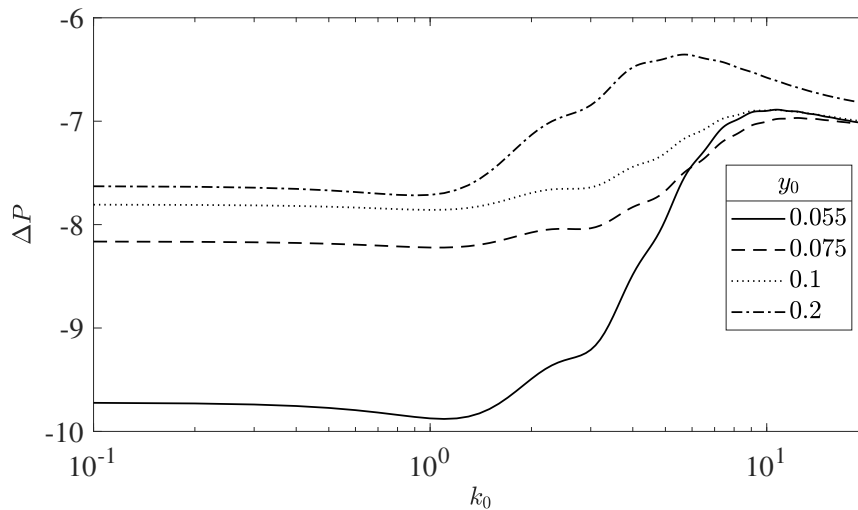


Fig. 3 ΔP for a near-field quadrupole source at $x_0 = 0.95$ and various y_0 . Negative values indicate the owl is quieter than the buzzard by that many dB.

and for the buzzard:

$$\alpha_H^{\text{buzz}} = 0.22 \left(\frac{x}{2} + \frac{1}{2} \right)^{0.48}, \quad (11)$$

recalling that our chord lies in the region $x \in [-1, 1]$.

B. Bio-inspired results

We now present the acoustic results for the bio-inspired spanwise variations. Figure 3 shows the difference in far-field noise, $\Delta P = P^{\text{owl}} - P^{\text{buzz}}$ for P defined by (6), generated for a near-field quadrupole source located at (x_0, y_0) which models a turbulent trailing-edge source. Unsurprisingly, the owl is predicted to produce less trailing-edge noise than the buzzard since the trailing-edge of the owl's wing is far more porous (has a higher α_H value) than that of the buzzard's. This is particularly true for low-frequencies which are known to be significantly reduced by porosity [23]. However, the total level of low-frequency noise reduction is intrinsically linked to the vertical location of the quadrupole source. At higher frequencies, the owl is predicted to produce only 7 dB less trailing-edge noise, and this is similar across all quadrupole locations.

Figure 4 shows the effects of the owl versus buzzard distributions on leading-edge noise, and we see surprisingly that the owl-distribution produces less leading-edge noise despite the two wings having similar leading-edge porosity values. We consider an incident gust by selecting a potential satisfying $\partial \phi_1 / \partial y|_{y=0} = -e^{i\delta x}$, where $\delta = k_1 / \sqrt{1 - M^2}$, and $k_1 = \sqrt{1 - M^2} k_0 / M$ thus the Helmholtz number, k_0 , is δM , such that the gust convects from upstream with the mean

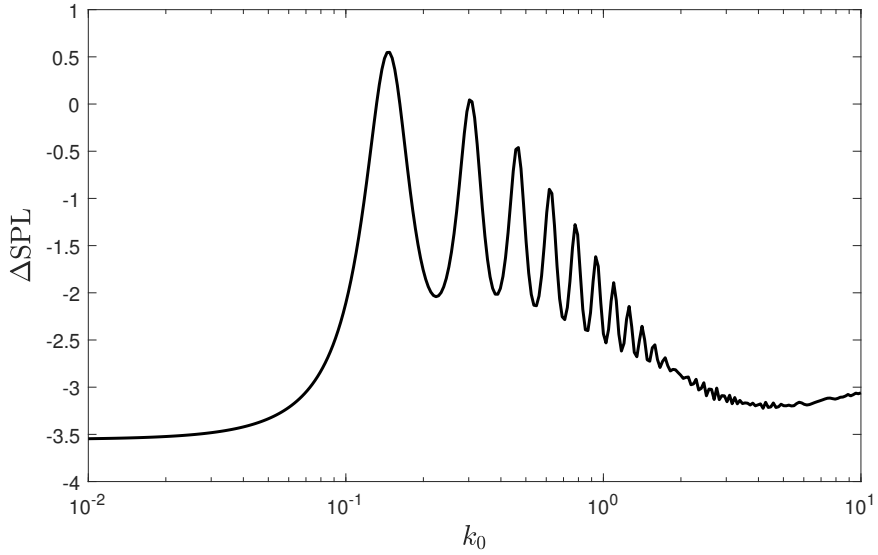


Fig. 4 ΔP for an incident gust. Negative values indicate the owl is quieter than the buzzard by that many dB.

flow with Mach number M . Full details of why this is the case may be found readily in the literature for leading-edge noise [36, 37]. We assume the same impedance style boundary condition, (1), noting that here the low Mach number approximation has been used. The difference in leading-edge noise levels is given in Figure 4, for $M = 0.05$. We notice that, again, the owl is quieter than the buzzard for low frequencies. However, now the reduction is only approximately 3.5 dB. Note the frequency range difference between the trailing-edge noise and the leading-edge noise; trailing-edge noise is a high-frequency phenomenon, whilst leading-edge noise is more dominant at lower frequencies. The lowest frequency flyover noise reductions [38] of 3 dB are in agreement with our leading-edge noise reduction predictions. However, it is unclear how much noise produced during the flyover tests can be attributed to each edge.

C. Monotonic distributions

We now investigate the effect of the precise distribution of porosity in the interior of the plate on trailing-edge noise. We consider varying porosity along a flat plate through the model

$$\alpha_H(x) = \alpha_L + (\alpha_T - \alpha_L) \left(\frac{x}{2} + \frac{1}{2} \right)^\gamma, \quad (12)$$

where $\alpha_{L,T}$ denote the open area ratios at the leading and trailing edge respectively. We consider only the case $\alpha_T \geq \alpha_L$, whereby the trailing edge has the same or greater porosity than the leading edge, as is observed from our wing measurements, and choose values of $\alpha_{L,T}$ representative of those measured for the owl.

We first consider the effect of varying the leading-edge porosity value, α_L , for fixed $\gamma = 2$ and fixed $\alpha_T = 0.3$ in Figure 5. If $\alpha_L \neq 0$, the effect of increasing the porosity at the leading edge is to uniformly reduce the noise across all frequencies, due to the increasing average porosity of the total plate. However, specifically $\alpha_L = 0$ opposes this trend at low frequencies, where the noise is reduced versus even a plate with a constant higher porosity of $\alpha_T = 0.3$.

The fact that this trend alters at low frequencies where the plate is acoustically compact is not unexpected. For impermeable plates, back scattering from the leading edge [39] is a significant contributor to the total far field noise. This back scattering arises because a non-zero jump in pressure across the plate at the leading edge must be smoothly reduced to zero upstream of the plate. If the leading-edge is porous, $\alpha_L > 0$, the back scattering is much weaker than if $\alpha_L = 0$, since there is communication between the upper and lower surfaces of the plate and the pressure jump across the plate at the (porous) leading edge is dampened [4]. This gives rise to two possible reasons for noise reduction at low frequencies as we vary γ ; increased average plate porosity and back scattering effects result in edge-to-edge interference.

For our variable porosity plate, in all cases of $\alpha_L > 0$ the back scattering and hence edge-to-edge interference may be neglected since the leading-edge porosity dampens the jump in surface pressure, and we hypothesise that the overall

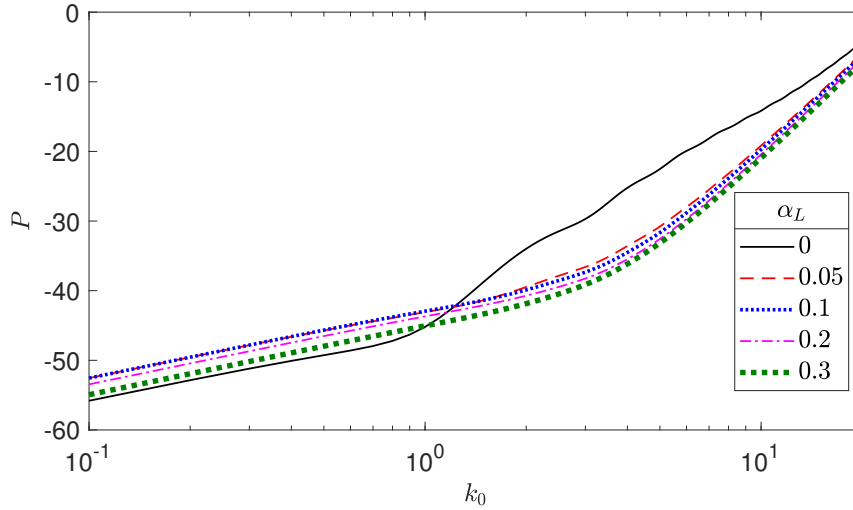


Fig. 5 Effect of varying α_L on trailing-edge noise over a range of frequencies. In all cases the porosity at the trailing edge is fixed at $\alpha_T = 0.3$.

acoustic behaviour depends only on the relative average porosity, thus mimics the high-frequency behaviour. For a plate with an impermeable leading edge, the back scattering cannot be neglected, and thus generates an additional acoustic source at the leading edge. Depending on the relative source strength of these sources, at a given frequency when the two sources are out of phase they will destructively interfere to result in a lower total amount of far-field noise. Similarly, if the back scattering is in phase, additional noise will be created. We illustrate this feature by considering the jump in surface pressure along the plate in Figure 6. There is a clear pressure jump induced near the leading edge for $\alpha_L = 0$, which is not present for porous leading edges even when the porosity is very small.

We investigate the effect of γ on this pressure jump near the leading edge in Figures 7 and 8 for low and high frequencies. Both real and imaginary parts of the pressure jump are now given. At low frequencies for small γ , the pressure jump near the leading edge is dominated by a negative real part. However, as γ increases the imaginary part near the leading edge increases. Therefore, the relative phase difference between the fields alters, and an optimal γ value should exist whereby the fields are in optimal destructive interference with each other. This is in contrast to the back scattering for a fully impermeable plate, whereby we found the respective pressure jump across the plate to be always positive for low frequency $k_0 = 0.5$, and only a fixed interference can be achieved.

At the higher frequency, $k_0 = 5$, the real and imaginary parts of $[p]$ in Figures 7 and 8 are both oscillatory and similar in magnitude across all values of γ . This is very similar to what would be observed for a full impermeable plate in Figure 9. We, therefore, expect that at high frequencies any back scattering effects for a variable porous plate with an impermeable leading edge are similar to those observed for a fully impermeable plate, namely that the magnitude of the back scattering is significantly reduced [39] and does not play a key role in the overall far-field noise.

Our results, therefore, corroborate the hypothesis that low-frequency behaviour is dominated by back scattering when the leading edge is rigid, and high-frequency behaviour is dominated by average plate porosity. This neglects the possibility of surface wave source cut-off, for which a more detail numerical study would be required to fully validate our hypothesis in case these surface waves may also play a role.

V. Conclusions

We considered the aeroacoustic effects of plates with chordwise varying porosity distributions. We have measured the distributions from two species of bird; the barn owl and the common buzzard, and matched their chordwise varying air flow resistance to an effective open area ratio as arises in the acoustic theoretical modelling of perforated plates. The noise reduction observed is in agreement with previous experimental results for uniformly porous plates, and is shown to be similar to that measured during flyover tests. However, the theory over-predicts that seen in laboratory tests. This is most likely due to additional features on the owl's wing that promote silent flight such as serrations and a downy upper coat. These features have not been modelled here.

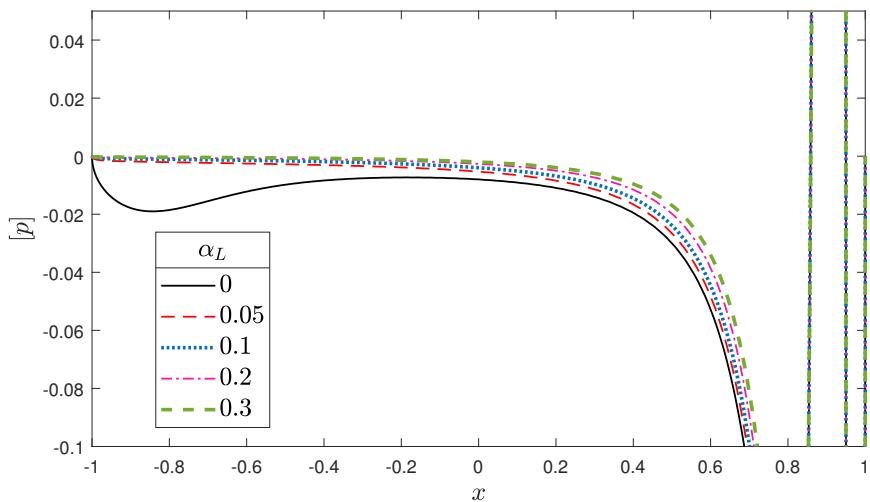


Fig. 6 Effect of varying α_L on the jump in (real) surface pressure, $[p]$ for $k_0 = 0.5$. In all cases the porosity at the trailing edge is fixed at $\alpha_T = 0.3$, and $\gamma = 2$.

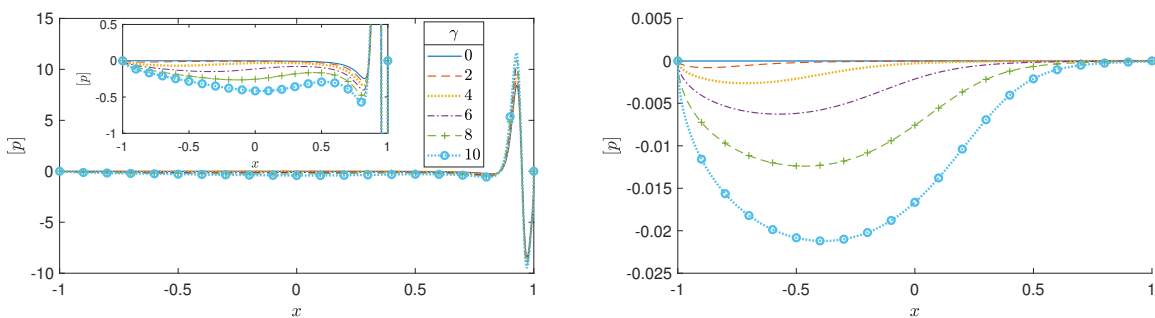


Fig. 7 Effect of varying γ on the jump in surface pressure, $[p]$, for $k_0 = 0.5$. Left shows the real part of $[p]$, right the imaginary part. In all cases the porosity at the trailing edge is fixed at $\alpha_T = 0.3$, and at the leading edge at $\alpha_L = 0$.

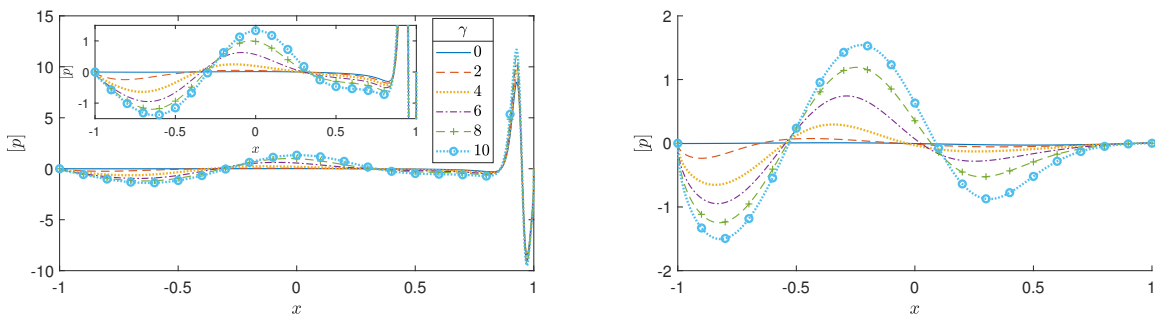


Fig. 8 Effect of varying γ on the jump in surface pressure, $[p]$, for $k_0 = 5$. Left shows the real part of $[p]$, right the imaginary part. In all cases the porosity at the trailing edge is fixed at $\alpha_T = 0.3$, and at the leading edge at $\alpha_L = 0$.

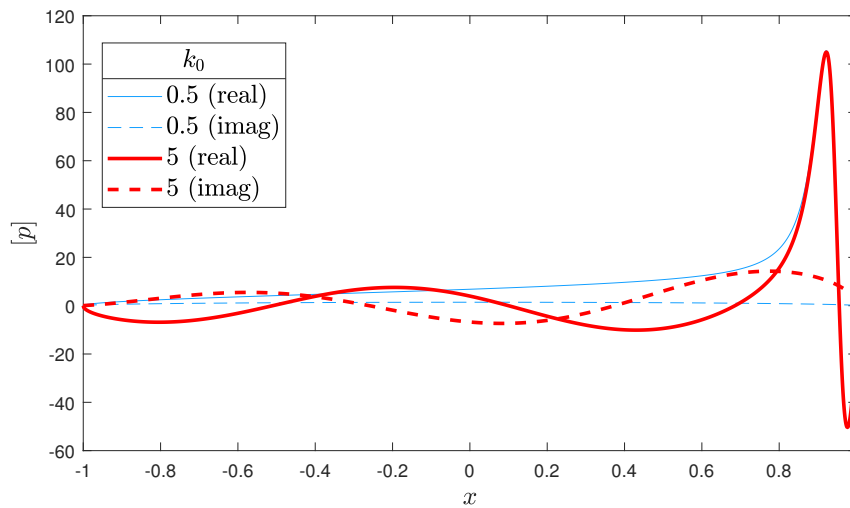


Fig. 9 Jump in surface pressure, $[p]$, for $k_0 = 0.5, 5$ in the case of an impermeable plate, $\alpha_H = 0$.

A further study of the effects of general monotonic streamwise distributions was then undertaken. It is seen that for low frequencies, a monotonic variation from a porous trailing edge to an impermeable leading edge can be more acoustically beneficial than if the plate remained at the constant trailing-edge porosity. This is attributed to the leading edge back scattered field [39]; an impermeable leading edge has a strong back scattered field which is able to destructively interfere with the trailing-edge field. At high frequencies, the back scattered field is both weaker and of much higher frequency.

References

- [1] Ayton, L., "Acoustic scattering by a finite rigid plate with a poroelastic extension," *Journal of Fluid Mechanics*, Vol. 791, 2016, pp. 414–438.
- [2] Geyer, T. F., Sarradj, E., and Giesler, J., "Application of a beamforming technique to the measurement of airfoil leading edge noise," *Advances in Acoustics and Vibration*, Vol. 2012, 2012.
- [3] Roger, M., Schram, C., and De Santana, L., "Reduction of airfoil turbulence-impingement noise by means of leading-edge serrations and/or porous material," *19th AIAA/CEAS aeroacoustics conference*, 2013, p. 2108.
- [4] Chaitanya, P., Joseph, P., Chong, T. Z., Priddin, M., and Ayton, L. J., "On the noise reduction mechanisms of porous airfoil leading edges," *Journal of Sound and Vibration*, Vol. 485, No. 115574, 2020.
- [5] Geyer, T. F., Sarradj, E., and Fritzsche, C., "Measurement of the noise generation at the trailing edge of porous airfoils," *Exp Fluids*, Vol. 48, 2010, pp. 291 – 308.
- [6] Geyer, T. F. and Sarradj, E., "Self Noise Reduction and Aerodynamics of Airfoils With Porous Trailing Edges," *Acoustics*, Vol. 1, Multidisciplinary Digital Publishing Institute, 2019, pp. 393–409.
- [7] Paruchuri, C., Joseph, S. P.-C. P., Priddin, M., and Ayton, L., "Downstream Perforations for the Reduction of Turbulence-Aerofoil Interaction Noise: Part I - Experimental Investigation," *preprint*, 2021.
- [8] Priddin, M., Ayton, L., Paruchuri, C., Palleja-Cabre, S., and Joseph, P., "Downstream Perforations for the Reduction of Turbulence-Aerofoil Interaction Noise: Part II - Theoretical Investigation," *preprint*, 2021.
- [9] Cavalieri, A. V. G., Wolf, W. R., and Jaworski, J. W., "Numerical solution of acoustic scattering by finite perforated elastic plates," *Proc. Roy. Soc. A*, Vol. 472, 2016.
- [10] Bae, Y. and Moon, Y. J., "Effect of passive porous surface on the trailing-edge noise," *Physics of Fluids*, Vol. 23, No. 12, 2011, pp. 126101.

- [11] Colbrook, M. J. and Ayton, L. J., “A spectral collocation method for acoustic scattering by multiple elastic plates,” *Journal of Sound and Vibration*, Vol. 461, 2019, pp. 114904.
- [12] Rienstra, S. and Peake, N., “Modal scattering at an impedance transition in a lined flow duct,” *11th AIAA/CEAS Aeroacoustics Conference*, 2005, p. 2852.
- [13] Iosilevskii, G., “Aerodynamics of permeable membrane wings,” *Eur. J. Mech. B Fluids*, Vol. 30, No. 5, 2011, pp. 534 – 542.
- [14] Hajian, R. and Jaworski, J. W., “The steady aerodynamics of aerofoils with porosity gradients,” *Proc. Roy. Soc. A*, Vol. 473, No. 2205, 2017, pp. 20170266.
- [15] Colbrook, M. J. and Priddin, M. J., “Fast and spectrally accurate numerical methods for perforated screens (with applications to Robin boundary conditions),” *IMA Journal of Applied Mathematics*, Vol. 85, No. 5, 2020, pp. 790–821.
- [16] Colbrook, M. J. and Kivil, A. V., “A Mathieu function boundary spectral method for scattering by multiple variable poro-elastic plates, with applications to metamaterials and acoustics,” *Proceedings of the Royal Society A*, Vol. 476, No. 2241, 2020, pp. 20200184.
- [17] Colbrook, M. J., Ayton, L. J., and Fokas, A. S., “The unified transform for mixed boundary condition problems in unbounded domains,” *Proc. Ro. Soc. A*, Vol. 475, No. 2222, 2019, pp. 20180605.
- [18] Colbrook, M. J. and Ayton, L. J., “Do we need non-linear corrections? On the boundary Forchheimer equation in acoustic scattering,” *Journal of Sound and Vibration*, Vol. 495, 2021, pp. 115905.
- [19] Ayton, L. J., Colbrook, M. J., Geyer, T. F., Chaitanya, P., and Sarradj, E., “Reducing aerofoil–turbulence interaction noise through chordwise-varying porosity,” *Journal of Fluid Mechanics*, Vol. 906, 2021.
- [20] Graham, R. R., “The silent flight of owls,” *Aeronaut. J*, Vol. 38, No. 286, 1934, pp. 837–843.
- [21] Lilley, G., “A study of the silent flight of the owl,” *4th AIAA/CEAS aeroacoustics conference*, 1998, p. 2340.
- [22] Colbrook, M. J., “Mathieu Function Collocation,” *github (online) <https://github.com/MColbrook/MathieuFunctionCollocation>*, 2020.
- [23] Jaworski, J. W. and Peake, N., “Aerodynamic noise from a poroelastic edge with implications for the silent flight of owls,” *J. Fluid Mech.*, Vol. 723, 2013, pp. 456–479.
- [24] Howe, M. S., Scott, M. I., and Sipic, S. R., “The influence of tangential mean flow on the Rayleigh conductivity of an aperture,” *Proc. Roy. Soc. A*, Vol. 452, No. 1953, 1996, pp. 2303–2317.
- [25] Rayleigh, L., *The Theory of Sound*, vol. 2. Dover, 1945.
- [26] Howe, M. S., *Acoustics of Fluid-Structure Interactions*, Cambridge Monographs on Mechanics, CUP, 1998.
- [27] Olver, F. W. J., Lozier, D. W., Boisvert, R. F., and Clark, C. W., *NIST handbook of mathematical functions*, Cambridge university press, 2010.
- [28] McLachlan, N. W., *Theory and application of Mathieu functions*, Dover Publications, Inc., New York, 1964.
- [29] Boyd, J. P., *Chebyshev and Fourier spectral methods*, Courier Corporation, 2001.
- [30] ISO 9053, “Acoustics-materials for acoustical applications-determination of air-flow resistance,” 1991.
- [31] Nachtigall, W. and Klimbingat, A., “Messung der Flügelgeometrie mit der Profilkamm-Methode und geometrische Flügelkennzeichnung einheimischer Eulen,” *Biona-report*, Vol. 3, 1985, pp. 45–86.
- [32] Bachmann, T., Mühlenbruch, G., and Wagner, H., “The barn owl wing: an inspiration for silent flight in the aviation industry?” *Bioinspiration, Biomimetics, and Bioreplication*, Vol. 7975, International Society for Optics and Photonics, 2011, p. 79750N.
- [33] Bachmann, T., Wagner, H., and Tropea, C., “Inner vane fringes of barn owl feathers reconsidered: morphometric data and functional aspects,” *J. Anat.*, Vol. 221, 2012, pp. 1–8.
- [34] Bachmann, T., Klän, S., Baumgartner, W., et al., “Morphometric characterisation of wing feathers of the barn owl *Tyto alba* pratincola and the pigeon *Columba livia*,” *Front. Zool.*, Vol. 4, 2007, pp. 23.

- [35] Chen, K., Liu, Q., Liao, G., Yang, Y., Ren, L., Yang, H., and Chen, X., “The Sound Suppression Characteristics of Wing Feather of Owl (*Bubo bubo*),” *Journal of Bionic Engineering*, Vol. 9, No. 2, 2012, pp. 192 – 199.
- [36] Tsai, C.-T., “Effect of airfoil thickness on high-frequency gust interaction noise.” 1992.
- [37] Ayton, L. J. and Kim, J. W., “An analytic solution for the noise generated by gust–aerofoil interaction for plates with serrated leading edges,” *Journal of Fluid Mechanics*, Vol. 853, 2018, pp. 515–536.
- [38] Sarradj, E., Fritzsche, C., and Geyer, T. F., “Silent owl flight: bird flyover noise measurements,” *16th AIAA/CEAS Aeroacoustics Conference*, 2010, pp. 2010–3991.
- [39] Moreau, S. and Roger, M., “Backscattering correction and further extensions of Amiet’s trailing-edge noise model. Part II: Application,” *J Sound Vib*, Vol. 323, 2009, pp. 397–425.

Acknowledgments

The work here has been funded by EPSRC Early Career Fellowship EP/P015980/1 (LJA), and EPSRC grant EP/L016516/1 (MJC). PC would like to acknowledge the financial support of the Royal Academy of Engineering (RF/201819/18/194). The authors also acknowledge the help of Christoph Fritzsche and Thomas Drescher with the acquisition of the wings and the air flow resistivity measurements as well as Dr. Martin Päckert and Jens Ziegler of the *Senckenberg Naturhistorische Sammlungen Dresden* for the preparation of the wings.